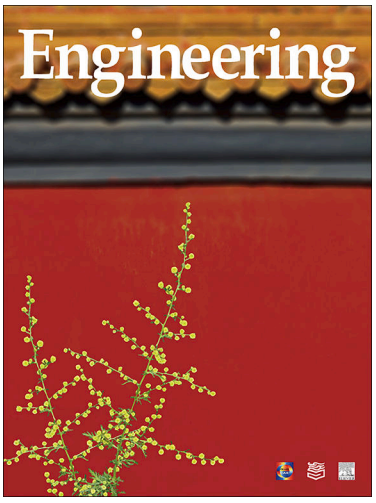
Journal Pre-proofs



Article

Prediction of the Thermodynamic Properties of Carbon-Free Flue Gases from Hydrogen-Powered Engines

Bo Chen, Yimin Xuan

PII: S2095-8099(26)00134-7
DOI: https://doi.org/10.1016/j.eng.2026.03.006
Reference: ENG 2289

To appear in: *Engineering*

Received Date: 29 June 2025
Revised Date: 13 February 2026
Accepted Date: 5 March 2026

Please cite this article as: B. Chen, Y. Xuan, Prediction of the Thermodynamic Properties of Carbon-Free Flue Gases from Hydrogen-Powered Engines, *Engineering* (2026), doi: https://doi.org/10.1016/j.eng.2026.03.006

This is a PDF of an article that has undergone enhancements after acceptance, such as the addition of a cover page and metadata, and formatting for readability. This version will undergo additional copyediting, typesetting and review before it is published in its final form. As such, this version is no longer the Accepted Manuscript, but it is not yet the definitive Version of Record; we are providing this early version to give early visibility of the article. Please note that Elsevier's sharing policy for the Published Journal Article applies to this version, see: https://www.elsevier.com/about/policies-and-standards/sharing#4-published-journal-article. Please also note that, during the production process, errors may be discovered which could affect the content, and all legal disclaimers that apply to the journal pertain.

© 2026 THE AUTHORS. Published by Elsevier LTD on behalf of Chinese Academy of Engineering and Higher Education Press Limited Company

Journal Pre-proofs

Research

Green Aviation Propulsion—Article

Prediction of the Thermodynamic Properties of Carbon-Free Flue Gases from Hydrogen-Powered Engines

Bo Chen, Yimin Xuan*

School of Energy and Power Engineering, Nanjing University of Aeronautics and Astronautics, Nanjing, 210016, China

*Corresponding author.
E-mail address: ymxuan@nuaa.edu.cn (Y. Xuan)

Abstract

Hydrogen-powered engines generate carbon-free flue gases with water vapor as their main combustion product. Under extreme temperature and pressure conditions, water vapor exhibits pronounced non-ideal gas behavior, resulting in thermophysical properties with significant pressure dependency. Concurrently, radiative heat transfer is strongly influenced by pressure-induced spectral line broadening and the high optical thickness that results from elevated water vapor concentrations. Existing thermophysical correlations are generally valid only within limited operating envelopes and lack the theoretical justification needed to reliably extend predictions to high-temperature regimes. Furthermore, conventional weighted-sum-of-gray-gases (WSGG) models rarely account for specific hydrogen-powered engine conditions. Most existing WSGG models employ coupled variables, in which pressure and concentration effects are lumped into a single pressure-path-length product, making them inadequate for capturing complex independent dependencies. In this study, sensitivity analyses of key thermophysical parameters were conducted to identify the parameters' functional dependence on temperature and pressure, yielding predictive models for specific enthalpy, heat capacities, and viscosity that enable physically consistent extrapolation to temperatures exceeding 2000 K. For radiative characteristics, a unified hydrogen-oriented WSGG (H-WSGG) framework was developed that decouples the nonlinear influences of water vapor concentration and total pressure, treating temperature, pressure, concentration, and path length as fully independent variables. Unlike conventional methods, these nonlinear effects are explicitly integrated into the absorption coefficients and weighting factors. Based on this framework and the Brayton cycle characteristics, two practical models were derived: the constant-pressure H-WSGG-C model and the constant-concentration H-WSGG-T model. Validation against original data and line-by-line (LBL) calculations under non-isothermal and non-uniform conditions demonstrate that the proposed thermophysical models achieve high accuracy and the H-WSGG models exhibit strong agreement with LBL benchmarks.

Keywords Carbon-free flue gases; Thermal radiation; Thermal properties; WSGG

1. Introduction

As the global energy structure transitions toward low-carbon development, the replacement of aviation power systems with clean energy sources is emerging as a key direction for promoting the sustainable development of green aviation [1]. Among these energy sources, hydrogen (H_2) fuel—with its carbon-free emissions, excellent mass-energy density, and diverse production pathways—is regarded as the most promising alternative to aviation kerosene [2–4]. Compared with conventional aeroengines, hydrogen-powered engines do not emit carbon dioxide (CO_2) during operation. The water vapor (H_2O) content in carbon-free flue gases is significantly higher, and such gases' chemical composition and thermodynamic properties differ substantially from those of the flue gases produced by conventional fuel. To meet the operational requirements of hydrogen fuel, traditional aviation engines require targeted modifications and evaluation [5] or completely new designs [6]. Consequently, the gas thermal property models developed for hydrocarbon fuels are generally not applicable to hydrogen-powered engines. In this context, the development of high-precision thermal property models for hydrogen-powered engines that couple multiple gas thermal parameters will become a critical foundational task for supporting flow field prediction, thermal load assessment, and overall engine performance optimization design.

As the content of water vapor in aeroengine flue gases increases, hydrogen aeroengines present new mechanical and heat-exchange design challenges. Under identical conditions, water vapor exhibits a specific heat at constant pressure (C_p) approximately twice that of carbon dioxide, as well as a specific enthalpy (h) about 2.5 to 4 times greater. However, its viscosity is only about 40% that of carbon dioxide [7]. Thus, the gas's heat storage capacity is significantly increased, enabling it to store more energy at the same temperature. This exacerbates the heat load on the combustion chamber and turbine blade surfaces. At the same time, the increase in enthalpy drop implies an increase in output work during expansion [8], which may cause component matching problems if the design is not adjusted accordingly. Additionally, the gas density and viscosity in hydrogen-powered engines differ from those in conventional aeroengines, which may alter the turbine flow field structure. Thus, the turbine channel design must be adjusted. Regarding thermal radiation, the higher degrees of freedom of water vapor molecules cause the radiation characteristics—especially the absorption coefficient—to show complex wavelength dependence over the entire spectral range [9]. Therefore, developing a thermophysical model that accounts for the independent effects of key aerothermal parameters is essential for the design of hydrogen-powered engines.

Journal Pre-proofs

In recent years, the development of models for thermodynamic properties has emerged as a prominent area of research, part[illegible]rties are diverse. Interpolation based on thermodynamic tables is affected by the interpolation algorithm and is limited in temperature and pressure range; when operating conditions fall outside the applicable range, prediction accuracy may decrease. Empirical correlations depend on the modeling approach and the specific application scenario. Complex equations, such as the International Association for the Properties of Water and Steam (IAPWS) standard [10,11], introduce additional computational overhead in computational fluid dynamics (CFD) simulations. Molecular dynamics methods [12] and machine-learning-based data-driven approaches [13] encounter high upfront computational costs and complex coupling with CFD solvers. For the prediction of thermal radiation, common methods for calculating radiative properties include the line-by-line method (LBL) model [14] based on spectral databases, the narrow-band correlation K model [15], and the weighted-sum-of-gray-gases (WSGG) model [16]. Among these, the spectral-based LBL method is the most accurate, as it calculates millions of spectral lines [17] in the spectrum to determine the emissivity. However, it requires exponentially more computational effort as the computational dimension increases, making it difficult to integrate with numerical methods in engineering. In contrast, the WSGG model represents the emissivity using a set of polynomials.

As it is able to achieve both accuracy and significantly improved computational efficiency, the WSGG model has been widely adopted. In order to broaden the model's applicability, prior studies have endeavored to integrate variables such as pressure and concentration into the WSGG model [18–24]. Cassol et al. [22] developed independent correlations for H_2O, CO_2, and soot, and then combined them to form WSGG correlations applicable to arbitrary mixing ratios. Wang and Xuan [18] introduced a pressure weighting factor into the standard WSGG model and investigated the effects of pressure on the radiative properties of aviation engine exhaust with an H_2O:CO_2 ratio of 1:1. Based on the statistical narrow-band (SNB) model, Shan et al. [19] incorporated the influence of pressure into both the absorption coefficients and the weighting factors of the gases.

Some WSGG models have been developed based on specific engineering applications. Kangwanpongpan et al. [25] and Bordbar et al. [26] concentrated on pure oxygen (O_2) combustion conditions. Xu et al. [27] developed new models for hydrogen-blended combustion conditions. Cai et al. [28] developed a new model to ascertain the radiative properties of carbon monoxide (CO), H_2O, and CO_2 mixtures within a coal powder gasification plant. Wang et al. [29] developed a novel WSGG model for aviation engine combustion chamber scenarios.

In addition, some studies have employed novel algorithms combining physics-informed neural networks (PINNs) [30] and genetic algorithms [31] to determine the WSGG coefficients. Most existing WSGG models are constructed for hydrocarbon fuels. The absorption coefficients for each gray gas are typically simplified to constants that are considered independent of external environmental parameters. The weighting factors primarily depend on temperature and generally do not account for multiple parameters. However, the environment in which hydrogen engine components are located varies significantly. The pressure variation in the combustion chamber area is relatively small, and the diffusion and incomplete mixing of combustion products result in a non-uniform concentration field. Moreover, the turbine and nozzle are accompanied by significant pressure gradients and temperature changes. Therefore, targeted corrections and optimizations must be carried out based on the operating characteristics of the different components.

In this work, a modeling framework is developed to investigate the thermophysical and radiative properties of carbon-free flue gases in hydrogen-powered engines. The study first examines the underlying modeling principles and employs sensitivity analyses to guide the formulation of thermodynamic models applicable to extended high-temperature regimes. Radiative characteristics are then addressed through the development of a hydrogen-oriented WSGG approach in which the total pressure and the water vapor concentration are treated as independent parameters. Based on the distinct operating features of the combustion chamber and turbine, corresponding modeling strategies are established for isobaric and constant-concentration processes. The resulting models are applied to analyze thermophysical and radiative behavior under a range of engine-relevant operating conditions.

2. Modeling and methods

In this section, the modeling mechanism and methodology are studied in terms of the thermodynamic and thermal radiation properties of carbon-free flue gases. Air has 78% nitrogen and 21% oxygen, with other components making up only 1%. Ignoring trace components, the air is considered to consist mainly of oxygen and nitrogen (N_2), with a ratio of O_2:N_2 = 1:3.76. It is assumed that all the oxygen is involved in the combustion process, nitrogen is not involved in the reaction, the products do not affect each other, and no additional reaction occurs. In the reaction equation (Eq. (1)), χ indicates the degree of hydrogen combustion.

$$H_2 + 0.5\chi\underbrace{(O_2 + 3.76N_2)}_{\text{Simplified Air}} \rightarrow \chi H_2O + (1-\chi)H_2 + 1.88\chi N_2 \quad (1)$$

Table 1 lists several specific scenarios. The final carbon-free flue gases consist of unreacted H_2 and N_2, along with the water vapor produced.

Table 1
Gas fractions (x) at different levels of hydrogen combustion.

Journal Pre-proofs

χ	x (N_2)		
100%	34.72%	0	65.28%
75%	31.12%	10.37%	58.51%
50%	25.77%	25.77%	48.46%

The thermodynamic properties of carbon-free flue gases are calculated as shown in Eq. (2), where x is the mole fraction of each gas species, g is the gas-species index, G is the total number of gas species in the mixture, and φ is the corresponding thermodynamic property. In this work, the main calculated properties are the specific enthalpy (h), the specific heat at constant pressure (C_p), the specific heat at constant volume (C_v), and the viscosity (vis).

$$\varphi_{\text{green}} = \sum_{g=1}^{G} x_{\text{gas},g}\varphi_{\text{gas},g} \quad (2)$$

The thermal radiation properties of carbon-free flue gases, including emissivity and radiation transfer, can be calculated using the WSGG model and its coupling with the radiation transfer equation (RTE). Hydrogen and nitrogen are transparent gases, so their effects on thermal radiation can be neglected. In contrast, the thermal radiation of water vapor cannot be neglected; thus, the thermal radiation of the carbon-free flue gases is mainly embodied by that of water vapor.

2.1 Thermodynamic property models of carbon-free flue gases

To determine the specific form of the thermodynamic property models for each component of carbon-free flue gases, the dependence of φ on temperature and pressure was analyzed using Eqs. (3) and (4), respectively.

$$\varphi_{\text{T}} = \left(\frac{\partial\varphi}{\partial T}\right)_{\text{P}} \quad (\varphi = h, C_{\text{p}}, C_{\text{v}}, \text{vis}) \quad (3)$$

$$\varphi_{\text{P}} = \left(\frac{\partial\varphi}{\partial P}\right)_{\text{T}} \quad (\varphi = h, C_{\text{p}}, C_{\text{v}}, \text{vis}) \quad (4)$$

For hydrogen, Fig. 1 presents an analysis of φ_{P} and φ_{T} based on finite-range data from the National Institute of Standards and Technology (NIST) [32]. The results in Figs. 1(a)–(d) indicate that the magnitude of φ_{P} is quite small. Moreover, at the temperature corresponding to $|\varphi_{\text{P}}|_{\max}$, the relative error between the extrema of φ_{P} remains below 0.23%, confirming its insensitivity to pressure variations. From the perspectives of thermodynamics and molecular thermal motion, the limited influence of pressure is also confirmed (see Section S1 in Appendix A). In addition, the required fuel–air ratio in the primary combustion zone of an aircraft engine tends to be slightly fuel-rich during takeoff, near stoichiometric during cruising, and slightly fuel-lean at high altitudes [33]. Consequently, the hydrogen content in carbon-free flue gases is generally low.

Journal Pre-proofs

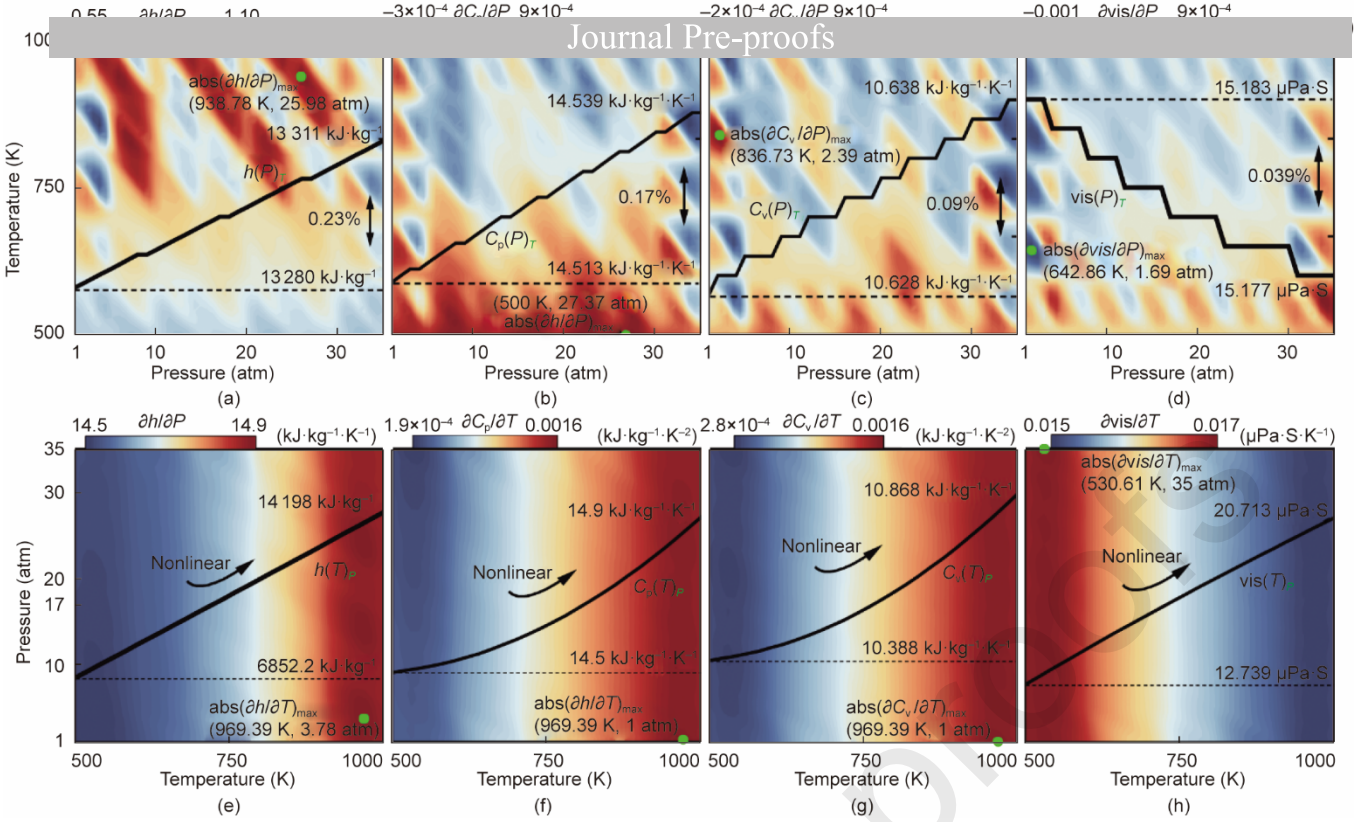


Fig. 1. Distribution of φ_{P} and φ_{T} in hydrogen. (a) $\partial h/\partial P$; (b) $\partial C_{\mathrm{p}}/\partial P$; (c) $\partial C_{\mathrm{v}}/\partial P$; (d) $\partial \mathrm{vis}/\partial P$; (e) $\partial h/\partial T$; (f) $\partial C_{\mathrm{p}}/\partial T$; (g) $\partial C_{\mathrm{v}}/\partial T$; (h) $\partial \mathrm{vis}/\partial T$. atm: standard atmosphere (unit of pressure). abs(• •) denotes the absolute value.

Based on the above analysis, this work treats hydrogen as an ideal gas and neglects its pressure effects. The base data of hydrogen are primarily derived from literature data under atmospheric pressure over a temperature range of 500–2000 K [8,34–36].

The models of hydrogen constructed in this work can be uniformly expressed by the generalized Eq. (5). C_{v} can be calculated using Mayer's formula [8], as shown in Eq. (6).

$$\varphi_{\mathrm{H_2}} = \sum_{i=0} \left(\frac{T}{T_{\mathrm{ref}}}\right)^{i} \left(\varphi_{\mathrm{H_2}} = h, C_{\mathrm{p}}, vis\right) \quad (5)$$

where $w_{\varphi,i}$ is the polynomial coefficient, i is the polynomial index, N is the upper limit of the summation index and the reference temperature $T_{\mathrm{ref}} = 500$ K.

$$C_{\mathrm{p,H_2}} - C_{\mathrm{v,H_2}} = R_{g,\mathrm{H_2}} \quad (6)$$

where R_g is the gas constant.

This work adopts the NIST [32] database as the main source for nitrogen's thermodynamic properties, covering a temperature range of 500–2000 K and pressures from 1 to 35 atm.

Figs. 2(a)–(d) shows the φ_{P} of nitrogen. As can be seen, the distribution of φ_{P} is relatively uniform, and its values are very small. At the temperature corresponding to $|\varphi_{\mathrm{P}}|_{\max}$, the relative error of the extrema of φ is less than 1%. As Fig. S1(b) in Appendix A shows, the variation in nitrogen's specific heat ratio with pressure remains minimal with increasing temperature. This information indicates indicate that the thermodynamic properties of nitrogen are relatively unaffected by pressure within the range of working conditions studied in this work. Therefore, the influence of pressure is neglected in this study.

Figs. 2(e)–(h) shows the φ_{T} of nitrogen. The values of φ_{T} vary significantly at different temperatures, indicating that φ is a nonlinear function of temperature. The solid line represents the variation in φ with temperature at the pressure corresponding to $|\varphi_{\mathrm{T}}|_{\max}$. The thermodynamic property values exhibit significant nonlinear changes as the temperature increases.

Journal Pre-proofs

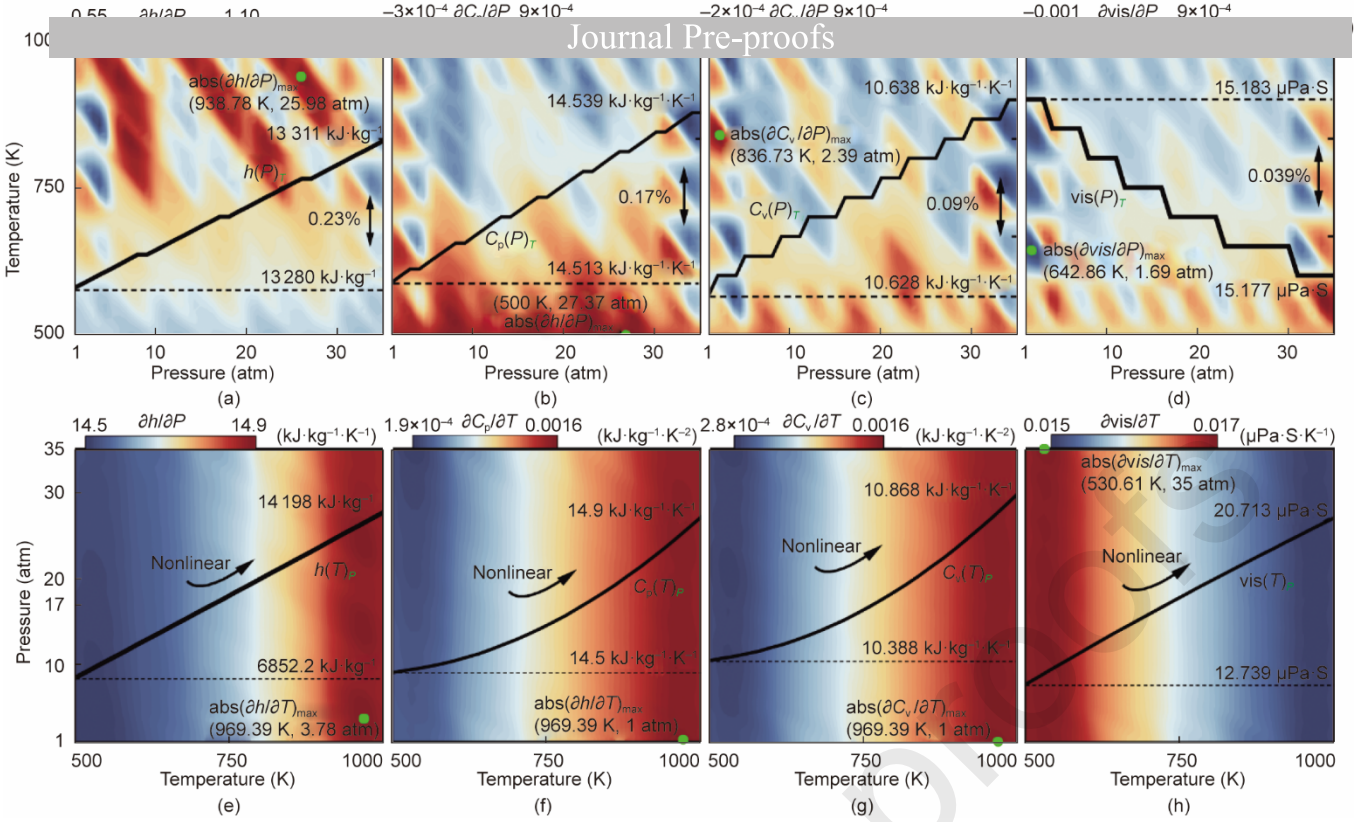


Fig. 2. Distribution of φ_{P} and φ_{T} in nitrogen. (a) $\partial h/\partial P$; (b) $\partial C_{\mathrm{p}}/\partial P$; (c) $\partial C_{\mathrm{v}}/\partial P$; (d) $\partial \mathrm{vis}/\partial P$; (e) $\partial h/\partial T$; (f) $\partial C_{\mathrm{p}}/\partial T$; (g) $\partial C_{\mathrm{v}}/\partial T$; (h) $\partial \mathrm{vis}/\partial T$.

Based on the above discussion, models for nitrogen were constructed, such as those shown in Eqs. (7) and (8).

$$\varphi_{\mathrm{N_2}} = \sum_{i=0}^{N} w_{\varphi,i}\left(\frac{T}{T_{\mathrm{ref}}}\right)^{i} \quad (\varphi = h, C_{\mathrm{p}}, C_{\mathrm{v}}) \quad (7)$$

$$\mathrm{vis}_{\mathrm{N_2}} = v_i T^{\frac{2}{3}} \quad (8)$$

where $w_{\varphi,i}$ is the polynomial coefficient to these models, $T_{\mathrm{ref}} = 500\ \mathrm{K}$ is the reference temperature, and v_i is the coefficient of the viscosity model.

The IAPWS has conducted extensive research on the thermodynamic properties of water vapor. This work employs the Gibbs-free-energy-based calculation methods (R7-97 [10] and R12-08 [11]) developed by the IAPWS to calculate the base data of water vapor. Specific calculations are described in Section S2 in Appendix A.

As shown in Fig. 3, φ_{P} and φ_{T} exhibit uniformly and highly nonuniformly distributed characteristics, respectively, across the entire temperature range, with no distinct boundary between the two regions. Figs. 3(a)–(d) shows that φ_{P} displays pronounced nonuniformity in the low-temperature range, indicating that the influence of pressure on φ varies with temperature and is more significant at lower temperatures. In contrast, $\varphi_{\mathrm{T}}(T)$ in Figs. 3(e)–(h) presents a multi-segment nonuniform distribution over the entire temperature range, with the most pronounced variations occurring between 520 and 1000 K; this suggests that the relationship between the variable and temperature is inconsistent across different ranges.

If a single functional relationship is used to perform a global fit of φ over the entire temperature range, the resulting surface would exhibit excessive curvature, resulting in significant local deviations. To improve the accuracy and stability of the model, a piecewise fitting approach is required to reduce the curvature within each subrange. In regions with relatively uniform distributions, the influence of pressure can be simplified, whereas the coupling between temperature and pressure in nonuniform regions should be strengthened. In the transitional zones (600–1000 K) connecting uniform and nonuniform regions, the pressure effect should be moderately weakened to balance model continuity and accuracy.

Specifically, for h and vis, the temperature range is divided into two segments with 1000 K as the boundary. Therefore, the generalized mathematical model for both can be divided into two segments: Eqs. (9) and (10), respectively.

$$\varphi_{\mathrm{H_2O},h,\mathrm{vis}} = \sum_{i=0}^{3}\sum_{j=0}^{3-i} w_{\varphi,ij}\left(\frac{T}{T_{\mathrm{ref}}}\right)^{i}\left(\frac{P}{P_{\mathrm{ref}}}\right)^{j} \quad T \in [520,1000]\ \mathrm{K} \quad (9)$$

where j is the polynomial index.

$$\varphi_{\mathrm{H_2O},h,\mathrm{vis}} = \sum_{i=0}^{3} w_{\varphi,i}\left(\frac{T}{T_{\mathrm{ref}}}\right)^{3-i} \quad T \in [1000,2000]\ \mathrm{K} \quad (10)$$

For C_{p} and C_{v}, φ_{P} and φ_{T} are uniformly distributed in the 1000–2000 K range, with only minor differences in their values. Thus, the influence of pressure can be neglected. As shown in Fig. 3(f), below 600 K, φ_{P} and φ_{T} exhibit the most pronounced variations and are highly sensitive to both temperature and pressure. The 600–1000 K range represents a

transitional zone, where the distribution of φ_P and φ_T gradually shifts from nonuniform to uniform, so the coupling effects of te[Journal Pre-proofs] (11) and (12).

$$\varphi_{\mathrm{H_2O},C_p,C_v} = \sum_{i=0}^{4}\sum_{j=0}^{4-i} w_{\varphi,ij}\left(\frac{T}{T_{\mathrm{ref}}}\right)^i\left(\frac{P}{P_{ref}}\right)^j \quad T \in [520,550] \cup [550,600] \cup [600,1000]\ \mathrm{K} \quad (11)$$

$$\varphi_{\mathrm{H_2O},C_P,C_V} = \sum_{i=0}^{4}\sum_{j=0}^{\min(1,4-i)} w_{ij}\left(\frac{T}{T_{\mathrm{ref}}}\right)^i\left(\frac{P}{P_{\mathrm{ref}}}\right)^j \quad T \in [1000,2000]\ \mathrm{K} \quad (12)$$

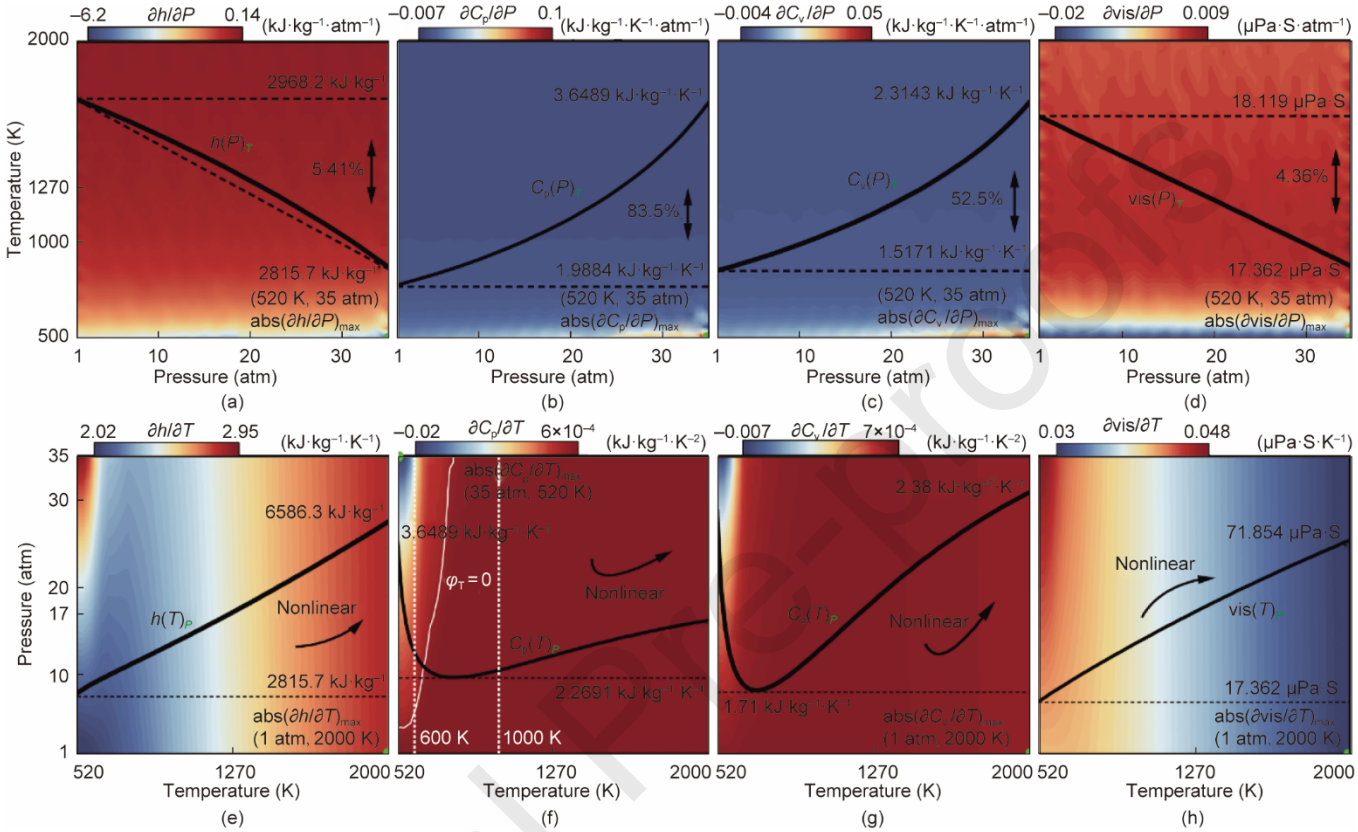


Fig. 3. Distribution of φ_P and φ_T in water vapor. (a) $\partial h/\partial P$; (b) $\partial C_p/\partial P$; (c) $\partial C_v/\partial P$; (d) $\partial \mathrm{vis}/\partial P$; (e) $\partial h/\partial T$; (f) $\partial C_p/\partial T$; (g) $\partial C_v/\partial T$; (h) $\partial \mathrm{vis}/\partial T$.

The coefficients in Eqs. (5), (7), and (8) for hydrogen and nitrogen can be solved directly using nonlinear fitting methods. The model coefficients are shown in Tables S1 and S2 in Appendix A. Eqs. (9)–(12), calculated in segments, using a nonlinear fitting method, yield the coefficients of the water vapor models. The results are shown in Tables S3 and S4 in Appendix A, respectively.

2.2 Thermal radiation models of carbon-free flue gases

2.2.1 Modeling mechanism

The standard WSGG model [16] is given as follows:

$$\varepsilon = \sum_{i=1}^{N} a_{\varepsilon,i}(T)[1 - \mathrm{e}^{-\kappa_i P_a L}] \quad (13)$$

where $a_{\varepsilon,i}(T)$ is the temperature weighting factor, κ_i is the absorption coefficient, P_a is the partial pressure, which can be obtained by multiplying the total pressure (P_t) and mole fraction x, and P_aL is the partial pressure path length of the gray gases. In Eq. (13), the total emissivity of the medium is calculated at atmospheric pressure, and the absorption coefficients for each gray gas component are assumed to be constant. The optimal precision of this method is constrained to hydrocarbon fuels with a constant molar ratio of H_2O to CO_2 at a constant pressure. Both P_aL and P_a are treated as single variables in the model, even though each represents a coupling of two original variables.

The coupling of variables has certain limitations. For example, when x and P_aL are fixed, the path length range can exhibit significant variations under different P_t, as shown in Table 2. This implies that a model optimized for a specific pressure may not cover the full range of path lengths encountered under other pressure conditions, thereby limiting its generality and accuracy. Moreover, as shown in Figs. 4 and 5, the absorption coefficient is not constant and varies nonlinearly with both water vapor concentration and total pressure.

Table 2

The path length range inferred under different total pressure conditions.

Journal Pre-proofs

P_t (atm)	x	P_a (atm)	P_aL (atm • m)	L range (m)
1	0.15	0.15	1×10^{-4} to 10	6.67×10^{-4} to 66.67
15	0.15	2.25	1×10^{-4} to 10	4.44×10^{-5} to 4.44
30	0.15	4.50	1×10^{-4} to 10	2.22×10^{-5} to 2.22

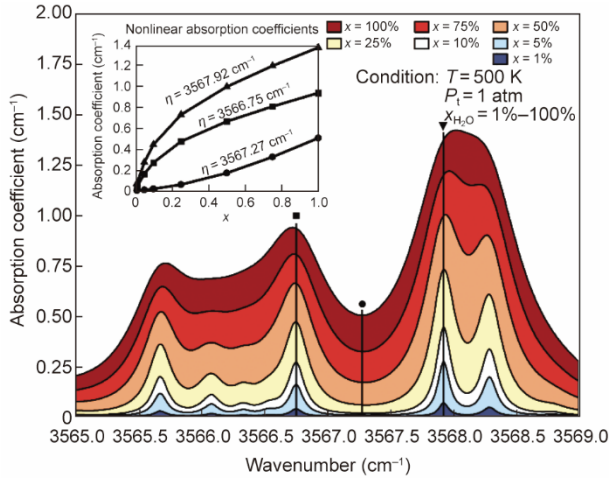


Fig. 4. Absorption coefficients at 3565–3569 cm^{-1} under different mole fractions.

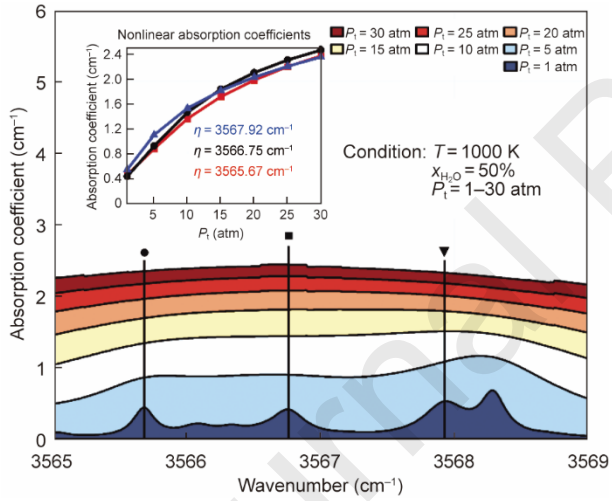


Fig. 5. Absorption coefficients at 3565–3569 cm^{-1} under different total pressures.

To address the aforementioned issues, the H-WSGG model developed in this work decouples P_aL into three independent variables: P_t, x, and L. Among them, P_t and x are related to specific application conditions. The hydrogen-powered engine cycle can be represented as a simplified Brayton cycle. Fig. 6 shows the construction principle and process of the H-WSGG. First, hydrogen combusts in the combustion chamber at essentially constant pressure during the 2–3 process in the Brayton cycle. The water vapor mole fraction inside the combustion chamber cannot be assumed to be constant, due to the non-homogeneous diffusion of combustion products and the continuous generation of water vapor. Second, carbon-free flue gases enter the turbine, expand to perform work, and experience a pressure drop. The amount of cooling gas is a small proportion of the main flow rate into the turbine [37], so it can be assumed that the variation in water vapor content within the turbine is minor; however, the change in pressure cannot be neglected.

The H-WSGG model includes four independent variables—T, P_t, x, and L—and is constructed using the control variable method. In H-WSGG-C, P_t is fixed at seven discrete values (Fig. S4 in Appendix A), while T, x, and L vary continuously at each fixed pressure, with weighting factors dependent on T and x and the effect of x incorporated into the absorption coefficient k. In H-WSGG-T, x is fixed at six discrete values (Fig. S5 in Appendix A), while T, P_t, and L vary continuously at each fixed x, with weighting factors dependent on T and P_t and the effect of P_t incorporated into k.

Journal Pre-proofs

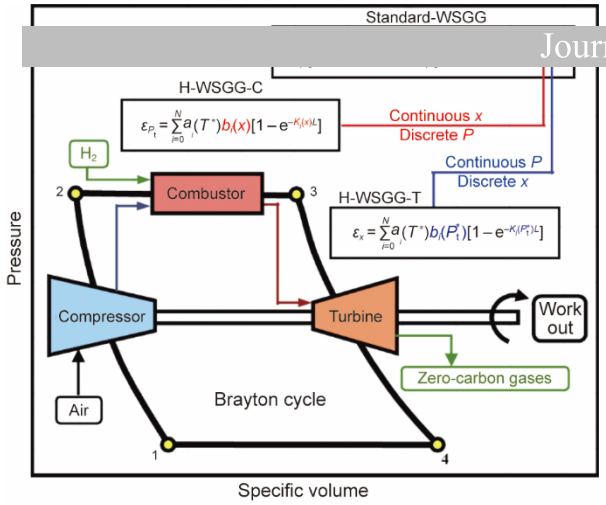


Fig. 6. Construction principle of the H-WSGG model.

The expression for the H-WSGG-C model is shown in Eq. (14), and the expanded form is shown in Eq. (15):

$$\varepsilon_{P_t} = \sum_{i=1}^{N} a_i(T^*) b_i(x)[1 - e^{-\kappa_i(x)L}] \quad (14)$$

$$\varepsilon_{P_t}(T,x,L) = \sum_{i=1}^{N} \underbrace{\sum_{j_1=0}^{J_1} \alpha_{i,j_1} (T^*)^{j_1}}_{T \text{ weight factor}} \underbrace{\sum_{j_2=0}^{J_2} \beta_{i,j_2} x^{j_2}}_{x \text{ weight factor}} [1 - \exp(-L \underbrace{\sum_{j_3=0}^{J_3} \gamma_i x^{j_3}}_{\kappa})] \quad (15)$$

$$\alpha_{i,j_1} = \sum_{m=0}^{M} \lambda_{i,j_1,m} x^m \quad (16)$$

where $a_i(T^*)$ and $b_i(x)$ are the weighting factors, $T^* = T/T_{\text{ref}}$ ($T_{\text{ref}} = 2000$ K), $\kappa_i(x)$ is the absorption coefficient, L is the path length. j_1,j_2,j_3,m are the polynomial index. J_1,J_2,J_3,M are the upper limit of the summation index. $\alpha,\beta,\gamma,\lambda$ are the coefficients of these polynomials. In the weighting factor solution process, the coefficient α_{i,j_1} is obtained by fitting discrete mole fraction data. To establish a continuous relationship between α_{i,j_1} and x, Eq. (16) is used for the correlation process.

The expression for the H-WSGG-T model is shown in Eq. (17), and the expanded form is shown in Eq. (18):

$$\varepsilon_x = \sum_{i=1}^{N} a_i(T^*) b_i(P_t^*)[1 - e^{-\kappa_i(P_t^*)L}] \quad (17)$$

$$\varepsilon_x(T,P_t,L) = \sum_{i=1}^{N} \underbrace{\sum_{j_1=0}^{J_1} \alpha_{i,j_1} (T^*)^{j_1}}_{T\ weight\ factor} \underbrace{\sum_{j_2=0}^{J_2} \beta_{i,j_2} (P_t^*)^{j_2}}_{P\ weight\ factor} [1 - \exp(-L \underbrace{\sum_{j_3=0}^{J_3} \gamma_i P_t^{j_3}}_{\kappa})] \quad (18)$$

where $b_i(P_t^*)$ is the P_t weighting factor, $P_t^* = P_t/P_{t,\text{ref}}$ ($P_{t,\text{ref}} = 40$ atm). $k_i(P_t^*)$ is the absorption coefficient, taking into account the effect of total pressure. α,β,γ are the coefficients of these polynomials. Similarly, the T weighting factor coefficient α_{i,j_1} in Eq. (18) must have a continuous relationship with P, as in Eq. (19).

$$\alpha_{i,j_1} = \sum_{m=0}^{M} \lambda_{i,j_1,m} (P_t^*)^m \quad (19)$$

2.2.2 Methodology

This work studies five gray gases and one transparent gas. Fig. 7 shows the process of solving for unknown quantities in the H-WSGG model. The spectral data used for fitting can be calculated from the spectral database using the LBL method [14]. The H-WSGG-C model is fitted over wide ranges of temperature (500–2800 K), pressure (1–30 atm), path length (9–1000 cm), and water vapor concentration (20%–50%), covering most hydrogen combustion conditions. The H-WSGG-T model covers temperatures of 500–2500 K, pressures of 6–40.5 atm, path lengths of 9–1000 cm, and water vapor concentrations corresponding to the hydrogen combustion conditions, ranging from 25.77% to 34.72%, which correspond to hydrogen fractions ranging from 100% to 74%. Detailed calculation parameters and procedures are provided in Section S5 in Appendix A.

The coefficients of the H-WSGG model are determined using the Levenberg–Marquardt (LM) algorithm [38], which has been widely applied in studies [18,21,25,27] on nonlinear fitting problems for WSGG models. However, the fitting results are highly sensitive to the initial values. To address this issue and obtain globally optimal fitting results, a hybrid optimization strategy based on cyclic random initialization is employed in this work. In each iteration, the initial coefficient values are randomly selected from a uniform distribution within the range (0,1), and the LM algorithm is used for rapid and accurate nonlinear fitting. The relative error (ξ) between the fitted results (ε_{fit}) and the original data is used as the evaluation criterion,

and the iteration stops only when this criterion is satisfied. The detailed solution process and LM parameters (Table S5) are prov

Journal Pre-proofs

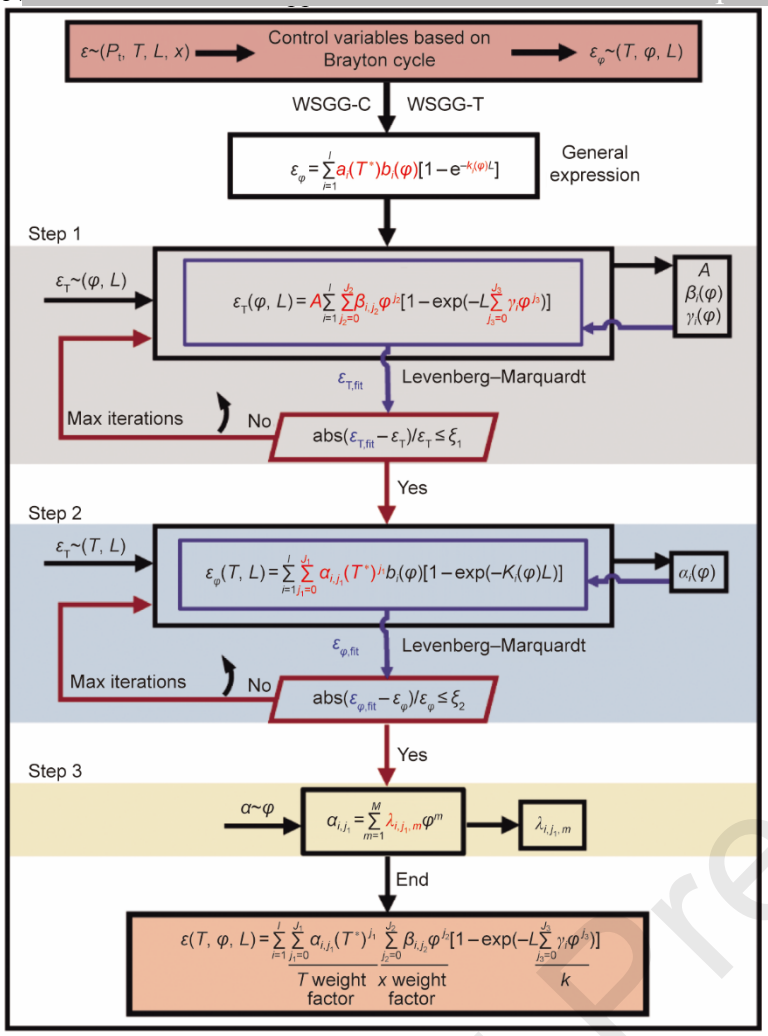


Fig. 7. Coefficient determination framework of the H-WSGG model. where abs(·) denotes the absolute value.

3. Results and discussion

3.1 Validation of the thermodynamic properties of carbon-free flue gas modeling

To evaluate the accuracy of the thermodynamic property modeling approach for each component of the carbon-free flue gases, the calculated results were compared with the original data used in model construction. The accuracy of the model (relative error, RE) was quantitatively assessed by comparing the relative error between the predicted values and the original data, as shown in Eq. (20):

$$RE = \left| \frac{\phi_{\text{model}} - \phi_{\text{original}}}{\phi_{\text{original}}} \right| \times 100\% \quad (20)$$

Fig. 8 shows the distribution of relative errors between the predicted data and the base data [8,34–36] used to construct the model for hydrogen at 1 atm and 500–2000 K. The predictions for C_p, h, and the viscosity align well with the original data. The RE_{max} for these three properties are 0.279%, 0.348%, and 0.431%, respectively. These values are all less than 0.5%, indicating that the model exhibits high predictive accuracy.

Journal Pre-proofs

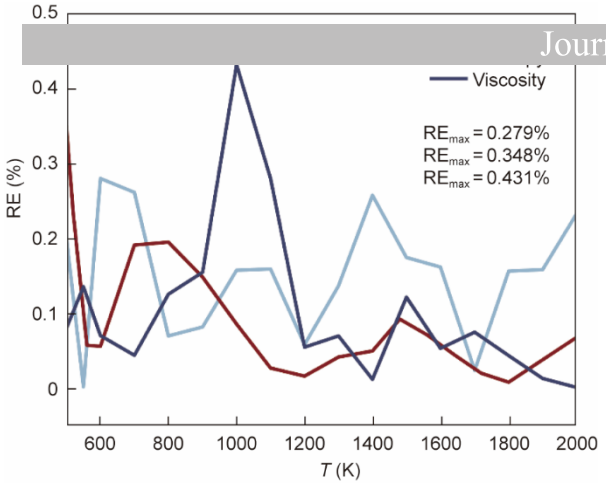


Fig. 8. Relative errors in the hydrogen thermodynamic property models.

Fig. 9 shows that, over the temperature range of 500–2000 K and pressure range of 1–35 atm, the maximum REs between the predicted data and the NIST data [32] for C_p, C_v, h, and viscosity in the model predictions are 0.854%, 0.360%, 0.170%, and 1.230%, respectively.

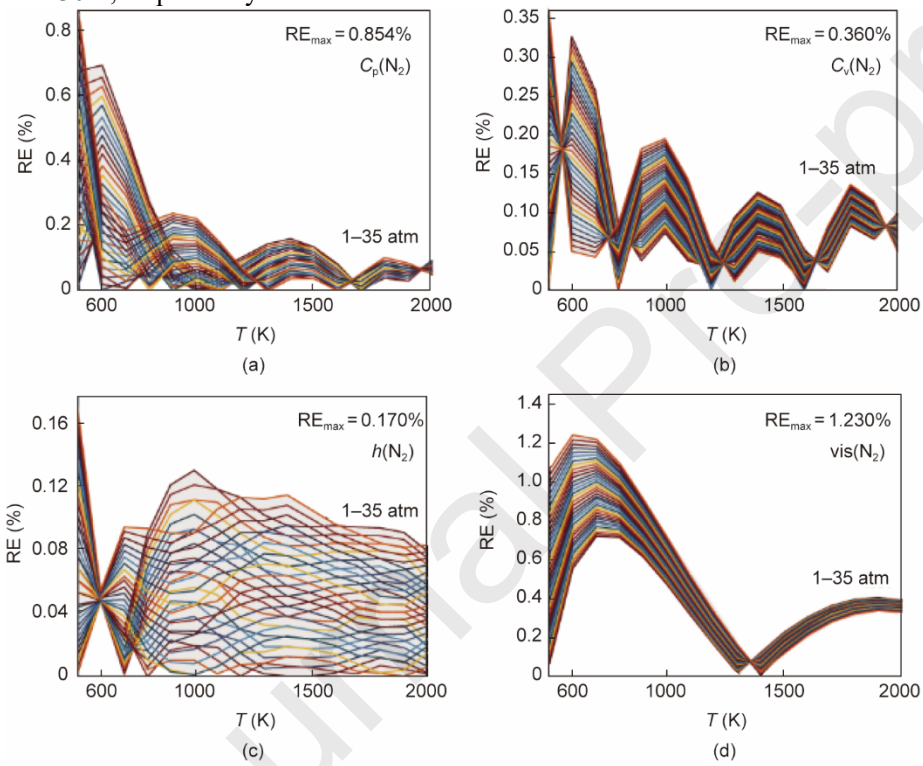


Fig. 9. Relative errors in the predicted nitrogen thermodynamic properties. (a) Relative errors of C_p; (b) Relative errors of C_v; (c) Relative errors of h; (d) Relative errors of vis.

Fig. 10 demonstrates the evaluation of the prediction accuracy of the water vapor thermodynamic property model across a temperature range of 500–2000 K and a pressure range of 1–35 atm. The maximum REs of the four key thermodynamic property parameters are all below 0.72% and the average REs are lower than 0.07%, compared with the results calculated using the IAPWS standard [10,11]

Journal Pre-proofs

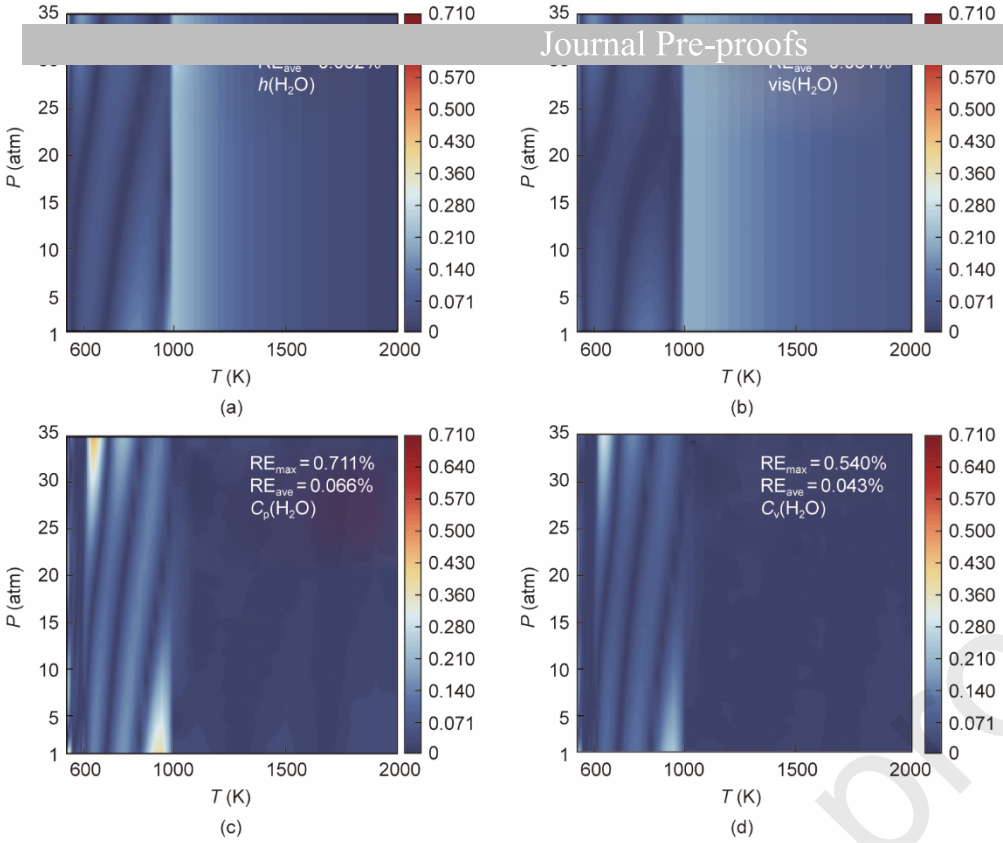


Fig. 10. Relative errors of the predicted thermodynamic properties of water vapor. (a) Relative errors of h; (b) Relative errors of vis; (c) Relative errors of C_P; (d) Relative errors of C_v.

3.2 Verification of emissivity results

The accuracy of the H-WSGG models in predicting emissivity was validated by comparing their results with LBL data over a temperature range of 500–2500 K, path lengths of 0.09–10 m, and various pressures and concentrations. The calculation results of the H-WSGG-C and H-WSGG-T models are presented in Figs. 11 and 12, respectively, with the mean RE under all operating conditions being less than 1% for both models. The maximum REs occur in regions with high temperatures and short path lengths. Because the H-WSGG model spans a wide range of temperatures (500–2500 K) and path lengths (0.09–10 m), it cannot fully capture nonlinear variations under extreme conditions. The fitted surface shows a large curvature near the boundary regions, resulting in larger errors. This issue can be addressed in future studies by constructing the model in a piecewise manner.

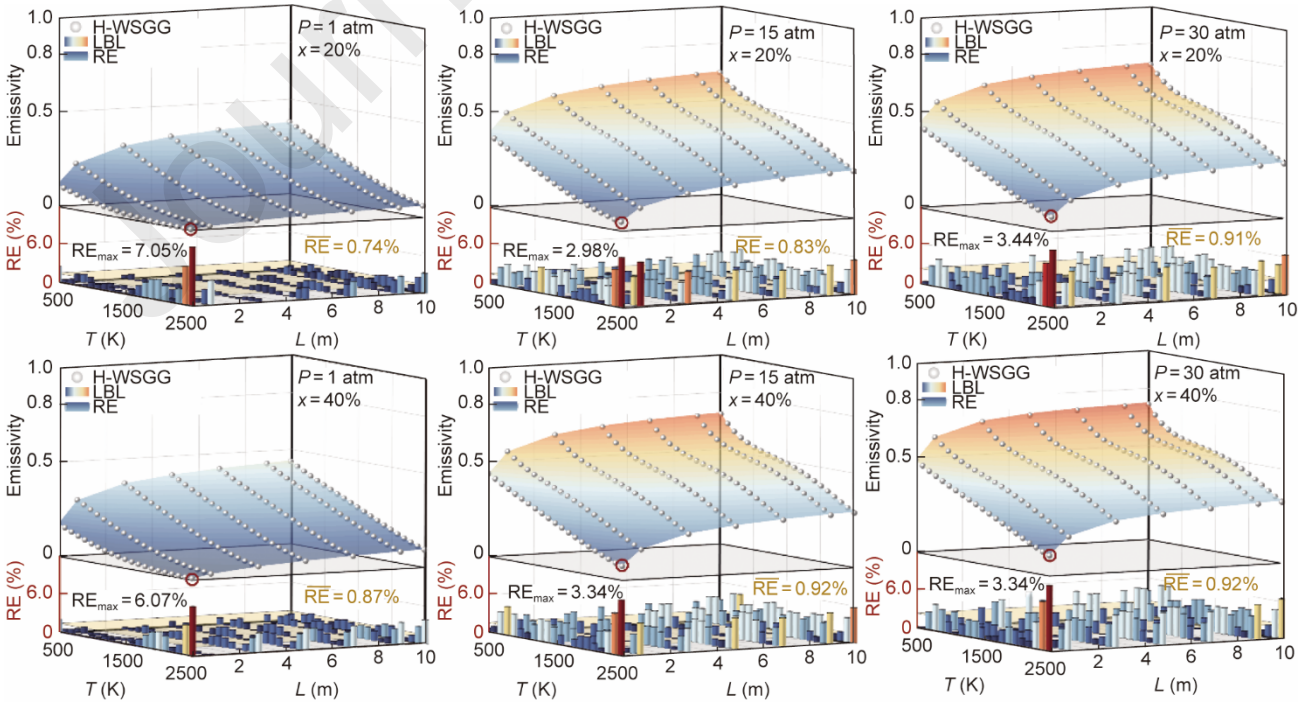


Fig. 11. H-WSGG-C emissivity calculation results and relative errors.

Journal Pre-proofs

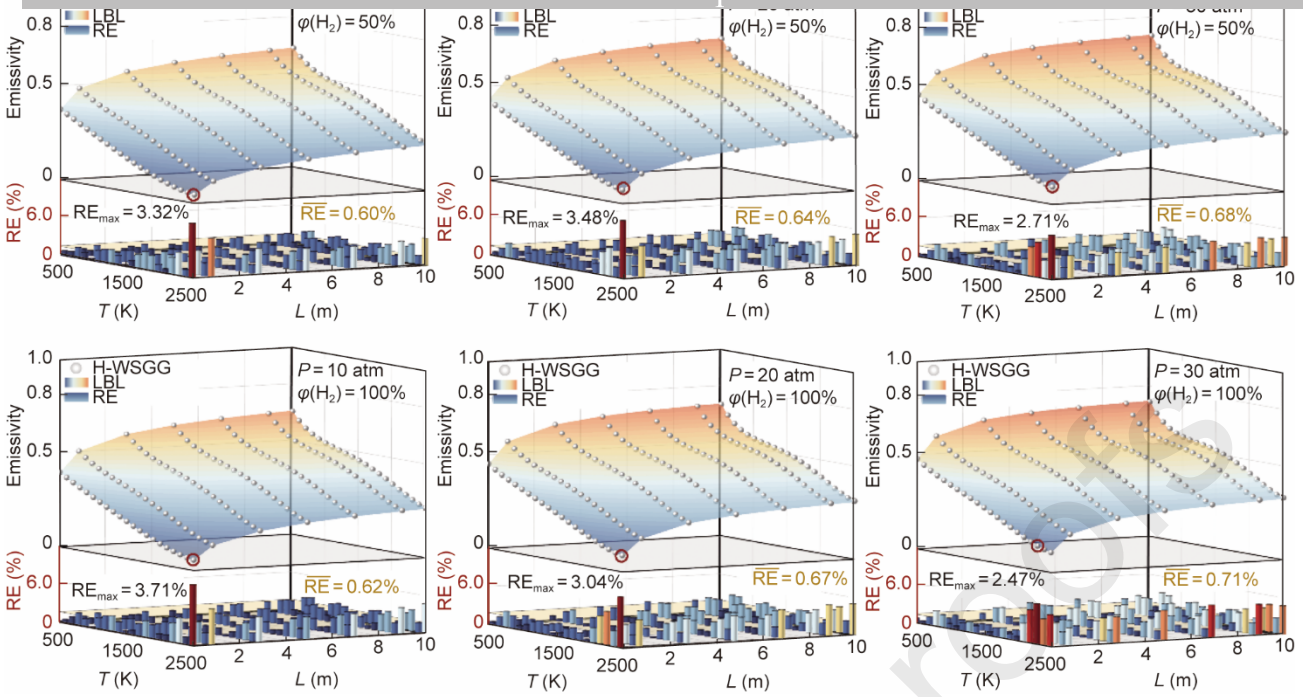


Fig. 12. H-WSGG-T emissivity calculation results and relative errors.

3.3 Solving the radiative transfer equation of the coupled H-WSGG model

Another application of the WSGG model involves coupling it with the RTE to solve for radiative heat flux and radiation source terms. To verify the feasibility of coupling the H-WSGG model with RTE, this work investigates thermal radiation transfer between one-dimensional (1D), infinitely parallel flat plates (Fig. 13). The distribution of radiative heat flux and radiative source terms between the flat plates is solved and compared with that of the LBL model as a benchmark.

The carbon-free flue gases are viewed as a completely absorbing and emitting, non-scattering medium. The resulting RTE is shown in Eq. (21) [39]:

$$\frac{\mathrm{d}I_\eta}{\mathrm{d}S} = \kappa_\eta (I_{b\eta} - I_\eta) \quad (21)$$

where S is the path length, I_η is the intensity of spectral radiation at η, $I_{b\eta}$ is the intensity of blackbody radiation, and κ_η is the absorption coefficient.

Eq. (22) shows the RTE for the ith gray gas coupled to the H-WSGG model:

$$\frac{dI_i}{ds} = \kappa_i (\omega_i I_b - I_i) \quad (22)$$

where I_i denotes the radiant intensity, κ_i is the absorption coefficient, ω_i is the weighting factor, the blackbody radiant intensity is $I_\mathrm{b} = \sigma T^4/\pi$, and σ is the Stefan–Boltzmann constant.

This work uses the discrete ordinates method (DOM) [39] with the S8 discrete format to solve Eqs. (21) and (22). The solution process is shown in Eqs. (S21)–(S28) in Section S7 in Appendix A.

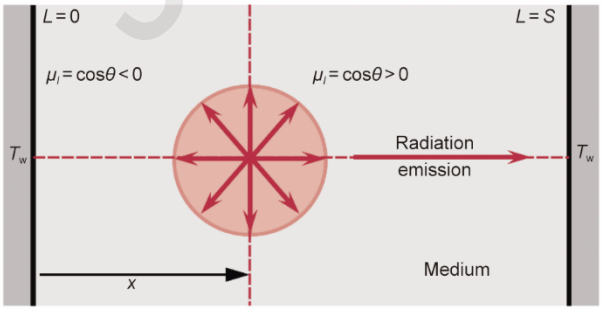


Fig. 13. The 1D infinity parallel plate schematic. where θ is the radiation angle, S is the length of the path.

The H-WSGG-C model's 1D examples include four non-isothermal, non-homogeneous cases, while the H-WSGG-T mod[Journal Pre-proofs]6 in Appendix A.

The numerical calculation results based on the H-WSGG model are then compared with the computational LBL model solutions. To quantitatively assess the accuracy of the coupled H-WSGG model RTE solution, the radiative heat flux (q) and radiation source term ($\dot{q}$) errors (δ) are defined as follows [22]:

$$\delta_{\text{flux}} = \frac{|q_{\text{H-WSGG}} - q_{\text{LBL}}|}{\max|q_{\text{LBL}}|} \times 100\% \quad (23)$$

$$\delta_{\text{source}} = \frac{|\dot{q}_{\text{H-WSGG}} - \dot{q}_{\text{LBL}}|}{\max|\dot{q}_{\text{LBL}}|} \times 100\% \quad (24)$$

Fig. 14(a), (b) shows the radiative heat flux and radiative heat source distributions for the H-WSGG-C model under four pressure conditions with nonlinear, continuous variation in temperature and water vapor concentration. The temperature increases continuously from 600 to 1800 K; the water vapor concentration increases from 20% to 45% from 0 to 0.5 m and the concentration then decreases symmetrically from 0.5 m to 1.0 m. Fig. 14(a) shows the thermal radiation transferring from the highest temperature point at 0.5 m to the low-temperature regions on both sides. Thus, the radiative heat flux at the midpoint is zero. The radiant heat flux on both sides of the midpoint is opposite. The negative sign indicates that the transfer paths are opposite the defined positive direction. Fig. 14(b) shows energy lost at the midpoint due to outward radiation and energy gained at both sides of the wall due to thermal radiation, indicating a symmetric distribution. The significant enhancement of radiative heat transfer with increasing pressure is due to the increase in the density of particles per unit volume when the pressure of the system increases. This increase leads to an increase in the optical thickness of the medium and intensifies the radiative transfer process.

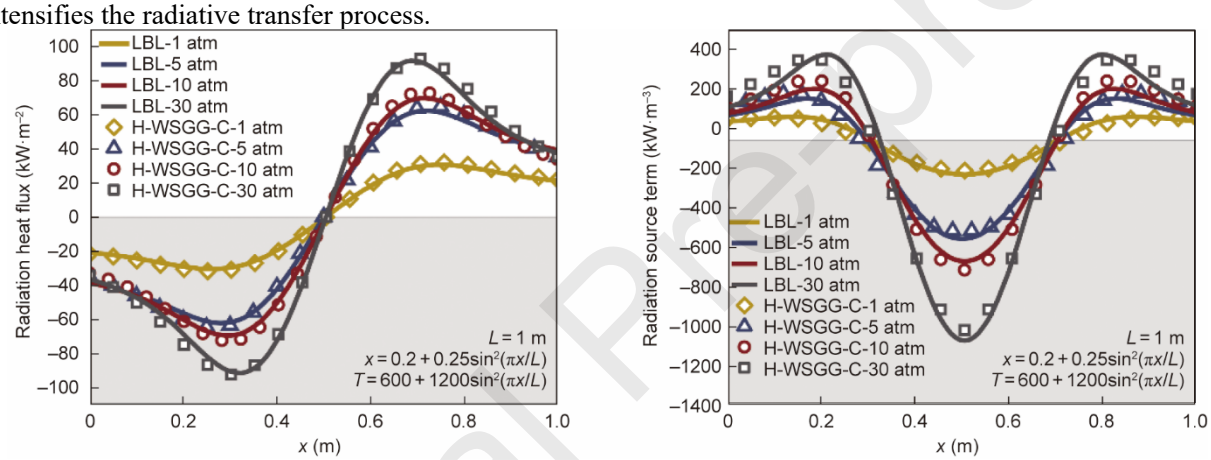


Fig. 14. Comparison of LBL and HWSGG calculations for non-homogeneous temperature and non-homogeneous concentration distributions. (a) Radiant heat flux; (b) radiation source term.

Figs. 15 and 16 respectively illustrate the distributions of the radiative heat flux and radiative heat sources for three hydrogen combustion scenarios accompanied by nonlinear, continuous changes in temperature and pressure. In the interval from 0 to 0.5 m, the pressure varies continuously from 10 to 15 atm, and the temperature rises continuously from 600 to 1800 K. In the interval from 0.5 to 1.0 m, the pressure and temperature decrease symmetrically. Fig. 15 shows that the distributions of the radiative heat flux are similar across different hydrogen combustion scenarios. However, the decrease in water vapor concentration has a smaller impact on the radiative heat flux.

Fig. 16 shows that the decrease in water vapor concentration reduces the absolute value of the radiation source term at 0.5 m. When x decreases from 34.72% to 25.77%, the absolute value of the radiation source term drops by 10.9%. This is because the decrease in water vapor concentration causes the particle number density per unit volume to decrease, resulting in a slight decrease in the optical thickness of the medium and weakening the radiative transfer process.

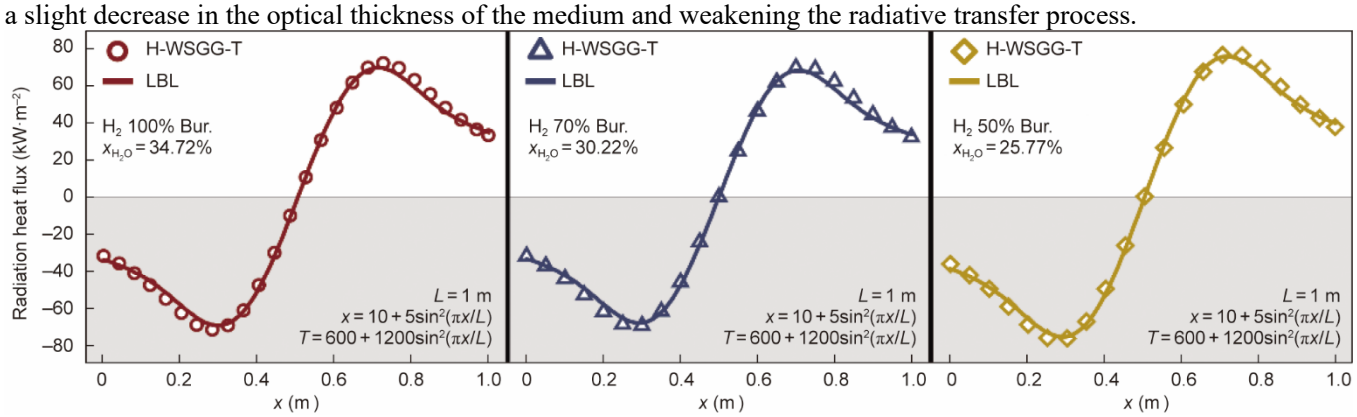


Fig. 15. H-WSGG-T radiation heat flux calculation results and relative error.

Journal Pre-proofs

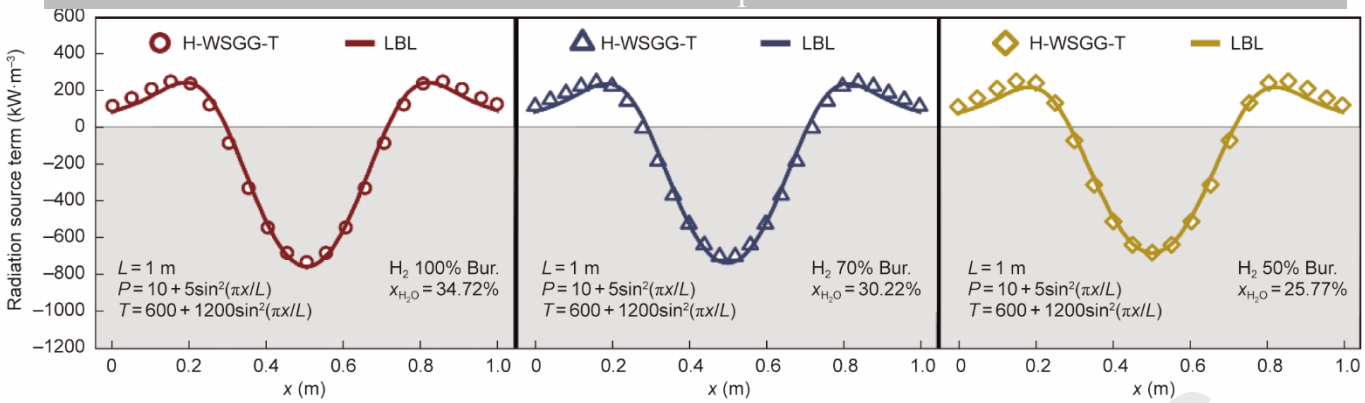


Fig. 16. H-WSGG-T radiation source term calculation results and relative error.

Table 3 lists the maximum and average relative error of the radiative heat flux, as well as the relative and average relative errors of the radiation source term at the midpoint, demonstrating good agreement with the reference results. The results show that the H-WSGG-C model effectively couples continuously varying water vapor concentration and temperature and is suitable for fixed-pressure combustion processes, while the H-WSGG-T model is suitable for conditions with varying temperature and pressure—particularly turbine operating conditions with relatively stable gas composition.

Table 3
Comparison of radiative heat flux and source term errors for H-WSGG.

Case	$\delta_{\text{flux-max}}$ (%)	$\delta_{\text{flux-ave}}$ (%)	$\delta_{\text{source-half}}$ (%)	$\delta_{\text{source-ave}}$ (%)
	1.6716	0.8940	8.3352	2.3198
Case 1.1	5.8644	1.5732	7.1820	2.3973
Case 1.2	8.0463	1.6346	6.5986	1.5853
Case 1.3	6.3101	1.7181	4.9204	2.0851
Case 1.4	6.9544	1.4879	0.4406	2.1514
Case 2.1	4.4076	1.1911	3.9806	1.5971
Case 2.2	8.6323	2.1537	3.1584	1.6370
Case 2.3				

4. Conclusions

This work developed a series of thermophysical property models for hydrogen-powered engine gases, including thermodynamic parameter models and H-WSGG radiation models. The maximum relative error for all predicted thermodynamic parameters of hydrogen was less than 0.5%. For nitrogen, the maximum relative errors were 0.854% for C_p, 0.360% for C_v, 0.170% for h, and 1.230% for viscosity. For water vapor, the maximum relative error for all predicted thermodynamic parameters was less than 0.72%. The H-WSGG models were specially optimized for aviation engines and are applicable to non-homogeneous environments with continuous changes of 500–2800 K and 20%–50%, as well as non-isobaric environments with continuous changes of 10–30 atm under oxygen-lean combustion (50%–100% O_2) at temperatures ranging from 500–2500 K. In non-homogeneous and non-isothermal combustion-chamber test cases, the maximum relative error for the radiative heat flux was 8.04%, and that for the radiative heat sources was 8.33%. In non-isothermal and non-isobaric test cases, the maximum relative error for the radiative heat flux was 8.63%, and that for the radiative heat sources was 3.98%. The thermal property model proposed in this study demonstrates good prediction accuracy under significant variations in temperature, pressure, and concentration. Thus, the series of thermophysical property models developed in this work are suitable for use in both thermodynamic analyses and radiation heat transfer simulations of hydrogen-powered engines.

Acknowledgements

This work was supported by Science and Industry Bureau Stable Support Funding “Forward-looking Strategic Research Project” (1002/ILD23003) and the Basic Science Center Program for Ordered Energy Conversion of the National Natural Science Foundation of China (No. 52488201)

References

Journal Pre-proofs

[1] Ansell PJ. Review of sustainable energy carriers for aviation: benefits, challenges, and future viability. Prog Aerosp Sci 2023;141:100919.
[2] Lei H, Khandelwal B. Hydrogen fuel for aviation, in: aviation fuels. Amsterdam: Elsevier, 2021. p. 237–70.
[3] Adler EJ, Martins JR. Hydrogen-powered aircraft: fundamental concepts, key technologies, and environmental impacts. Prog Aerosp Sci 2023;141:100922.
[4] Brewer GD. Hydrogen aircraft technology. London: Routledge; 2017.
[5] Yin H, Xuan Y, Lian W, Wang T. A comprehensive set of criteria for evaluating thermal management systems of aerial vehicles. Sci China Technol Sci 2023;66(7):2093–107.
[6] Cecere D, Giacomazzi E, Ingenito A. A review on hydrogen industrial aerospace applications. Int J Hydrogen Energy 2014;39(20):10731–47.
[7] Haynes WM. CRC handbook of chemistry and physics. Boca Raton: CRC Press; 2016.
[8] Qing F, Shiwu L, Li Z. Engineering thermodynamics. Xi'an: Northwestern Polytechnical University Press; 2006. Chinese.
[9] Howell JR, Mengüç MP, Daun K, Siegel R. Thermal radiation heat transfer. Boca Raton: CRC Press; 2020.
[10] Cooper J, Dooley R. Revised release on the IAPWS industrial formulation 1997 for the thermodynamic properties of water and steam. Report. Lucerne: The International Association for the Properties of Water and Steam (IAPWS); 2007.
[11] Huber ML, Perkins RA, Laesecke A, Friend DG, Sengers JV, Assael MJ, et al. New international formulation for the viscosity of H_2O. J Phys Chem Ref Data 2009;38(2):101–25.
[12] Raabe G. Molecular simulation studies on thermophysical properties. Berlin: Springer; 2017.
[13] Soltanian MR, Bemani A, Moeini F, Ershadnia R, Yang Z, Du Z, et al. Data driven simulations for accurately predicting thermodynamic properties of H_2 during geological storage. Fuel 2024;362:130768.
[14] Arnold J, Whiting E, Lyle G. Line by line calculation of spectra from diatomic molecules and atoms assuming a Voigt line profile. J Quant Spectrosc Radiat Transf 1969;9(6):775–98.
[15] Soufiani A, Taine J. High temperature gas radiative property parameters of statistical narrow-band model for H_2O, CO_2 and CO, and correlated-K model for H_2O and CO_2. Int J Heat Mass Transf 1997;40(4):987–91.
[16] Smith T, Shen Z, Friedman J. Evaluation of coefficients for the weighted sum of gray gases model. J Heat Transfer 1982;104(4):602–8.
[17] Rothman LS, Gordon I, Barber R, Dothe H, Gamache RR, Goldman A, et al. HITEMP, the high-temperature molecular spectroscopic database. J Quant Spectrosc Radiat Transf 2010;111(15):2139–50.
[18] Wang B, Xuan Y. An improved WSGG model for exhaust gases of aero engines within broader ranges of temperature and pressure variations. Int J Heat Mass Transf 2019;136:1299–310.
[19] Shan S, Qian B, Zhou Z, Wang Z, Cen K. New pressurized WSGG model and the effect of pressure on the radiation heat transfer of H_2O/CO_2 gas mixtures. Int J Heat Mass Transf 2018;121:999–1010.
[20] Johansson R, Leckner B, Andersson K, Johnsson F. Account for variations in the H_2O to CO_2 molar ratio when modelling gaseous radiative heat transfer with the weighted-sum-of-grey-gases model. Combust Flame 2011;158(5):893–901.
[21] Dorigon LJ, Duciak G, Brittes R, Cassol F, Galarça M, França FH. WSGG correlations based on HITEMP2010 for computation of thermal radiation in non-isothermal, non-homogeneous H_2O/CO_2 mixtures. Int J Heat Mass Transf 2013;64:863–73.
[22] Cassol F, Brittes R, França FH, Ezekoye OA. Application of the weighted-sum-of-gray-gases model for media composed of arbitrary concentrations of H_2O, CO_2 and soot. Int J Heat Mass Transf 2014;79:796–806.
[23] Bordbar H, Hyppänen T. Line by line based band identification for non-gray gas modeling with a banded approach. Int J Heat Mass Transf 2018;127:870–84.
[24] Bordbar H, Fraga GC, Hostikka S. An extended weighted-sum-of-gray-gases model to account for all CO_2-H_2O molar fraction ratios in thermal radiation. Int Commun Heat Mass Transf 2020;110:104400.
[25] Kangwanpongpan T, França FH, da Silva RC, Schneider PS, Krautz HJ. New correlations for the weighted-sum-of-gray-gases model in oxy-fuel conditions based on HITEMP 2010 database. Int J Heat Mass Transf 2012;55(25–26):7419–33.
[26] Bordbar MH, Węcel G, Hyppänen T. A line by line based weighted sum of gray gases model for inhomogeneous CO_2–H_2O mixture in oxy-fired combustion. Combust Flame 2014;161(9):2435–45.
[27] Xu J, Chen R, Meng H. WSGG models for radiative heat transfer calculations in hydrogen and hydrogen-mixture flames at various pressures. Int J Hydrogen Energy 2021;46(61):31452–66.
[28] Cai X, Shan S, Zhang Q, Zhao J, Zhou Z. New WSGG model for gas mixtures of H_2O, CO_2, and CO in typical coal gasifier conditions. Fuel 2022;311:122541.
[29] Wang C, Di H, Lin H, Shang S, Yang L. Applications of weighted-sum-of-gray-gas model with soot to an experimental aero-engine combustion chamber. Appl Therm Eng 2024;236:121511.
[30] Chen W, Yang R, Ren T, Zhao C. Development and validation of a physics-informed neural network-based WSGG model for multi-species gas mixtures. Int J Heat Mass Transf 2025;251:127328.
[31] Asllanaj F, Contassot-Vivier S, Pascale F, da Fonseca RJ, Fraga GC, França FH. Unified gas radiation model over the entire temperature range based on WSGG. Int J Heat Mass Transf 2025;241:126713.
[32] Linstrom PJ, Mallard WG. The NIST chemistry webbook: a chemical data resource on the Internet. J Chem Eng Data 2001;46(5):1059–63.
[33] Chuanjun Y, Wei F. Combustion. Xi'an: Northwestern Polytechnical University Press; 2005. Chinese.
[34] Weidao S, Jungeng T. Engineering thermodynamics. 4th ed. Beijing: Higher Education Press; 2005. Chinese.
[35] Holman JP. Heat transfer. 10th ed. New York City: McGraw-Hill Education; 2010.
[36] Incropera FP, DeWitt DP, Bergman TL, Lavine AS. Fundamentals of heat and mass transfer. New York City: Wiley New York; 1996.
[37] Bin Z, Shaobin L, Sheng Z, Shengqin H, Xueqi Z. Research progress on the aircraft engine air system bleeding. Adv Aeronaut Sci Eng 2012;3:476–85.
[38] Marquardt DW. An algorithm for least-squares estimation of nonlinear parameters. J Soc Ind Appl Math 1963;11(2):431–41.
[39] Modest MF. Radiative heat transfer. 3rd ed. Boston: Academic Press; 2013.

Declaration of Interest Statement

The authors declare that they have no known competing financial interests or personal relationships that could have appeared to influence the work reported in this paper.